Tissue-mimicking phantoms for performance evaluation of photoacoustic microscopy systems

HSUN-CHIA HSU, KEITH A. WEAR, T. JOSHUA PFEFER, ⓘ AND WILLIAM C. VOGT* ⓘ

Center for Devices and Radiological Health, U.S. Food and Drug Administration, 10903 New Hampshire Avenue, Silver Spring, MD 20993, USA
*william.vogt@fda.hhs.gov

Abstract: Phantom-based performance test methods are critically needed to support development and clinical translation of emerging photoacoustic microscopy (PAM) devices. While phantoms have been recently developed for macroscopic photoacoustic imaging systems, there is an unmet need for well-characterized tissue-mimicking materials (TMMs) and phantoms suitable for evaluating PAM systems. Our objective was to develop and characterize a suitable dermis-mimicking TMM based on polyacrylamide hydrogels and demonstrate its utility for constructing image quality phantoms. TMM formulations were optically characterized over 400–1100 nm using integrating sphere spectrophotometry and acoustically characterized using a pulse through-transmission method over 8–24 MHz with highly confident extrapolation throughout the usable band of the PAM system. This TMM was used to construct a spatial resolution phantom containing gold nanoparticle point targets and a penetration depth phantom containing slanted tungsten filaments and blood-filled tubes. These phantoms were used to characterize performance of a custom-built PAM system. The TMM was found to be broadly tunable and specific formulations were identified to mimic human dermis at an optical wavelength of 570 nm and acoustic frequencies of 10–50 MHz. Imaging results showed that tungsten filaments yielded 1.1–4.2 times greater apparent maximum imaging depth than blood-filled tubes, which may overestimate real-world performance for vascular imaging applications. Nanoparticles were detectable only to depths of 120–200 μm, which may be due to the relatively weaker absorption of single nanoparticles vs. larger targets containing high concentration of hemoglobin. The developed TMMs and phantoms are useful tools to support PAM device characterization and optimization, streamline regulatory decision-making, and accelerate clinical translation.

1. Introduction

Photoacoustic imaging (PAI) is a rapidly emerging technology that has shown promise in numerous preclinical and clinical applications including cancer detection, oximetry, vascular imaging, dermatology, and molecular imaging, owing to its capability of providing deep imaging of both endogenous and exogenous chromophores [1–4]. PAI is a highly scalable modality, and PAI systems can be generally categorized into macroscopic imaging systems (macro-PAI) and photoacoustic microscopy (PAM) systems based on their spatial resolution (∼ 0.1–1 mm vs. 1–50 μm) and imaging depth (∼ 2–5 cm vs. 1–5 mm) [5]. Macro-PAI has seen significant technological advances and translation over the last decade, including several commercial devices for research and investigational clinical use [6] as well as a recently FDA-approved clinical breast imaging system [7]. PAM has also seen rapid growth and development, although fewer commercial systems are available and no PAM devices have received FDA approval or clearance yet. Potential clinical applications for PAM include monitoring of skin conditions, melanoma detection, wound healing, and histological tumor margin assessment [8–12]. Currently, reported PAM device

designs vary substantially due to both the nascency of the technology and the breadth of potential clinical applications under investigation, each presenting different required specifications such as imaging throughput, image quality, and miniaturization [10,13–15]. Differences in key parameters including optical wavelengths, acoustic frequencies, optical-acoustic confocality, and scanning mechanisms are expected to have large impacts on device performance, increasing the need for standardized performance test methods to evaluate and compare performance of different devices. However, no consensus-based test methods are currently available for PAM device evaluation given the technology's nascent status. For mature imaging modalities like ultrasound, CT, and MRI, standardized test methods are available that make use of tissue-mimicking phantoms [16–18]. These phantoms are often composed of tissue-mimicking materials (TMMs) that simulate the intrinsic properties and/or idealized morphology of tissue. Development of robust phantom test methods for PAM has the potential to support device characterization and optimization, streamline regulatory evaluation, and accelerate clinical translation of PAM-based medical devices.

We first reviewed the literature to identify current practices in PAM image quality assessment as candidate methods. Commonly evaluated PAM image quality characteristics included spatial resolution (both axial and lateral), penetration depth, field of view, signal-to-noise ratio (SNR), image uniformity, and sensitivity, in order of relative frequency [13,14,19,20]. Typical resolution test methods included qualitative inspection of the smallest distinguishable line pairs of a water-immersed USAF target [21–23], edge/line spread function fitting over a sub-resolution particle or boundary such as a razor blade edge [24–26], single nanoparticle, or carbon fiber embedded in phantom materials [22,27,28]; maximum imaging depth was usually determined by measuring the greatest depth for which a slanted, high-contrast target or an array of multiple targets could be visualized. Commonly used targets include a black-painted needle [15,21,24], carbon fibers [27], tungsten filament [29], or black tape [22]. In addition, performance testing by direct imaging of in vivo animal tissue features such as blood vessels or externally inserted targets has been reported [24,27].

However, these common practices in PAM image quality test methodology have several limitations. First, most PAM image quality studies did not perform testing in phantoms composed of TMMs with well-characterized, biologically-relevant optical and acoustic properties. Many studies imaged targets immersed in water, which does not replicate the optical absorption, optical scattering, or acoustic attenuation of tissue. Scattering media such as Intralipid were occasionally used, but the optical and acoustic properties of the medium were often not characterized, and the optical absorption of Intralipid is expected to be much lower than that of most soft tissues. Some studies used ex vivo tissue such as chicken meat as the background medium, but this approach is expected to suffer from poor repeatability and reproducibility. Target inclusions were also rarely characterized, and common high-contrast targets (e.g., metal needles, carbon fiber) are expected to produce much stronger PA signals than endogenous absorptive targets such as blood vessels and may thus overestimate imaging performance. There is clearly an unmet need for a robust, well-characterized TMM suitable for constructing PAM image quality phantoms.

While most PAM phantom test methods we found in the literature did not incorporate biologically relevant TMMs, several TMMs have been previously developed for macro-PAI phantoms, including hydrogels [30–32], polyurethane [33], polydimethylsulfoxide (PDMS) [34], gel wax [35], and polyvinyl vinyl chloride (PVCP) [36,37]. Additives are typically incorporated into these materials to adjust optical absorption (e.g., dyes or pigments) and scattering (e.g., TiO_2 particles or Intralipid). TMM acoustic properties such as attenuation and speed of sound can be controlled by adjusting concentration of the base polymer/substrate [31,32,38], and attenuation can be increased by adding sub-acoustic resolution (~ 50 μm) particles such as glass microspheres [36,38]. Macro-PAI phantoms constructed from these TMMs generally include arrays of embedded targets such as sub-resolution filaments (~ 0.1–0.5 mm diameters) or fluid-filled tubes (~ 0.5–2 mm diameters) located at various depths [39].

However, macro-PAI TMMs and phantoms may not be suitable for PAM image quality assessment. Macro-PAI TMMs have typically only been characterized for lower acoustic frequencies used by macro-PAI systems (1–15 MHz), whereas their properties at PAM-relevant frequencies (up to 60 MHz) are unknown. Additionally, the degree of material homogeneity at the microscopic scale (e.g., dispersed light-scattering particles) for macro-PAI TMMs is unclear, as the lower spatial resolution of macro-PAI systems may reduce sensitivity to small-scale heterogeneity. Finally, the proposed phantom and target geometries in prior macro-PAI studies were generally incompatible with the resolution (< 10 µm), imaging depth (< 3 mm), and field of view (∼ 10 mm × 10 mm × 2 mm) of PAM devices. Macro-PAI phantoms typically contain relatively large inclusions positioned at depths of several centimeters, which are too deep to detect with PAM. Thus, there remains an outstanding need for TMMs and phantoms specifically designed for PAM systems.

In this study, our overall goal was to develop tissue-mimicking phantoms suitable for evaluating PAM system image quality. Given the prevalence of PAM research for dermatology applications, we developed a tunable polyacrylamide (PAA) hydrogel-based TMM simulating the optical and acoustic properties of human dermis. PAA offers fast and simple preparation, along with greater mechanical strength and longer shelf life than traditional agar/gelatin hydrogels [32]. We used this TMM to construct phantoms containing relevant imaging targets and demonstrated quantitative assessment of image quality characteristics of a custom-built PAM system. Owing to the broad range of reported dermis optical properties, we performed image quality testing in phantoms with low, medium, or high optical attenuation.

2. Materials and methods

2.1. TMM preparation

To develop a dermis-like TMM for PAM, we identified published values of optical absorption coefficient (μ_a), reduced scattering coefficient (μ_s'), acoustic attenuation coefficient (α), and speed of sound (c) for human dermis (Fig. 1) [40–48]. Reported data for these properties spanned a wide range, which reflects variations in tissue conditions (anatomical location, storage, and processing, etc.) and property measurement methodology. As our custom PAM system operates at an optical wavelength of 570 nm and acoustic frequencies of 15–50 MHz (Section 2.4), we chose ranges of TMM property values as shown in Table 1. As we intended to construct phantoms containing discrete blood vessel-mimicking inclusions, TMM optical properties were selected to represent bloodless dermis using reported ex vivo data (Table 2).

Table 1. Reported Ranges of Optical and Acoustic Properties of Human Skin.

μ_a (570 nm) (cm^{-1})	μ_s' (570 nm) (cm^{-1})	c (m/s)	α(40 *MHz*) (dB/cm)
0.87–2.1	16–35	1550–1740	45–115

We chose to develop phantoms based on PAA hydrogels, a TMM that has been recently demonstrated for image quality assessment of macro-PAI systems [32]. PAA hydrogels were formed by mixing 40% w/v, 19:1 acrylamide:bisacrylamide stock solution (J60909-K2, Alfa Aesar, Ward Hill, MA, USA) with deionized (DI) water, then degassing in a vacuum chamber for one hour. Optical and acoustic additives were then added, including water-soluble nigrosin (N4754, MilliporeSigma, St. Louis, MO, USA) to adjust optical absorption and 21 nm titanium oxide (TiO$_2$) nanopowder (718467, MilliporeSigma) to adjust optical scattering. Unlike previous PAA phantoms [32], those for PAM face more stringent requirements for controlling TMM uniformity at a microscopic scale, especially regarding TiO$_2$ particle aggregation. To alleviate the need for manual tumbling, we suspended TiO$_2$ particles by adding 30% v/v Tween 20 (P9416,
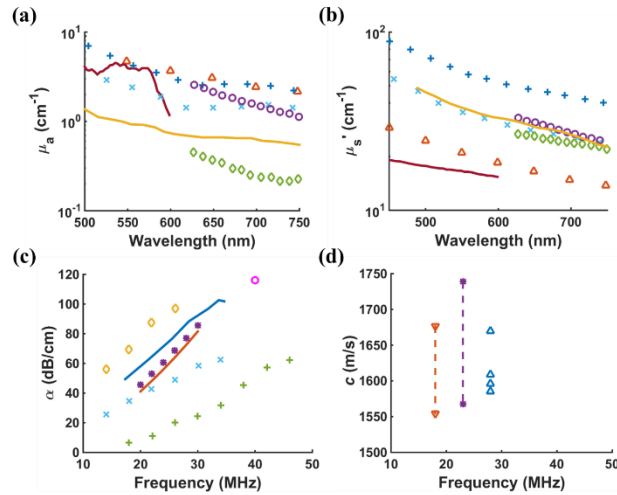
Fig. 1. Reported properties of human skin. (a, b) Optical absorption coefficient (μ_a) and reduced scattering coefficient (μ_s') of ex vivo Caucasian skin (triangle) [44], epidermis (plus sign) [42], and dermis (cross, diamond) [41,42]; in vivo skin averaged over different pigmentation levels (dark red line) [43]; ex vivo highly pigmented dermis (circle) [41] and Asian dermis (yellow line) [40]. (c, d) Acoustic attenuation coefficient (α) and speed of sound (c) of ex vivo breast skin (dark blue line and triangle) [45]; ex vivo dermis (orange line and down-pointing triangle) and epidermis (asterisk) [48]; in vivo forearm dermis (plus sign, circle) [46,47], fingertip dermis (diamond) [46], and subcutaneous fat (cross) [46]. Dash lines in (d) represent ranges.

Table 2. Target Optical Properties and Composition of Three TMM Formulations Used in Phantom Testing.

Total Volume = 10 mL	Low TMM	Medium TMM	High TMM
μ_a (570 nm) (cm^{-1})	1.3	1.8	2.0
μ_s' (570 nm) (cm^{-1})	14	19	22
nigrosin (% wt)	0.003% (0.3 mg)	0.0045% (0.45 mg)	0.005% (0.5 mg)
TiO$_2$ nanopowder (mg/mL)	0	0	1.2 (12 mg)
Tween 20 (% v/v)	20% (2 mL)	30% (3 mL)	30% (3 mL)
40% w/v 19:1 acrylamide:bisacrylamide stock solution (% v/v)	25% (2.5 mL)	25% (2.5 mL)	25% (2.5 mL)
APS (% w/v)	0.08% (8 mg)	0.08% (8 mg)	0.08% (8 mg)
TEMED (% v/v)	0.1% (10 μL)	0.1% (10 μL)	0.1% (10 μL)
DI water (% v/v)	54.9% (5.49 mL)	44.9% (4.49 mL)	44.9% (4.49 mL)

MilliporeSigma) to the acrylamide solution, followed by bath sonication for 30 minutes. Bright-field microscopy was used to assess TiO$_2$ dispersion, and potential changes in optical and acoustic properties due to addition of Tween 20 were also characterized. After these additives were mixed in the arcylamide solution, 0.08% w/v ammonium persulfate (APS) (A7460, MilliporeSigma) and 0.1% v/v N,N,N',N'-tetramethylethylenediamine (TEMED, T9281, MilliporeSigma) were added to initiate crosslinking, with gelation occurring within 20 minutes.

We characterized hydrogels with PAA monomer concentrations from 12% up to 30% w/v, above which samples presented significant shrinkage and reduced ductility in preliminary testing.

This likely resulted from temperature-induced phase transition in hydrogel due to excessive heat released from auto-acceleration of the polymerization reaction gel solution [49,50]. It may be possible to mitigate these auto-acceleration issues at high acrylamide concentration using suspension or emulsion polymerization techniques [51], but it will be shown that the achievable range of concentrations yielded adequate optical and acoustic tunability (Section 3). PAM imaging performance in tissue is expected to be highly dependent on optical attenuation, which reduces local fluence and resultant photoacoustic signal amplitude. To account for the high variation in reported optical properties of the dermis and thus uncertainty regarding TMM design, we prepared each of the two phantom designs using three different TMMs with low, medium, and high optical attenuation (Table 2, hereafter denoted as "low TMM", "medium TMM", and "high TMM"), and compared image quality test results between phantoms comprised of each TMM.

2.2. Acoustic and optical characterization

TMM acoustic properties were characterized using a broadband through-transmission substitution technique as described and validated previously [32,36,52,53]. TMM samples were formed in nontreated tissue cell culture flasks (08-772-1J, Thermo Fisher Scientific, Inc., Waltham, MA) and placed in the middle of two coaxially-aligned, broadband transducers (V317-SU, Olympus, Waltham, MA) submerged in degassed (DG), deionized (DI) water. A pulser/receiver (Panametrics 5900PR, Olympus) was used to drive the emitting transducer and acquire ultrasonic pulses transmitted through the samples and arriving at the receiving transducer. The received power was $P_s(f)$. Acoustic properties were measured at 4–8 locations per sample with 512 averaged measurements per location. A reference power, $P_w(f)$, was acquired by substituting a TMM-filled flask with a DG, DI water-filled flask. Water temperature was measured with a digital thermometer. Acoustic attenuation coefficient (α) vs. frequency (f) and speed of sound (c) were calculated as [36,52]:

$$\alpha_s(f) = \frac{10}{\Delta x} \log\left(\frac{P_w(f)}{P_s(f)}\right) + \alpha_w(f) \tag{1}$$

$$\alpha_w(f) = \frac{8.686 * 0.0215}{100} f^{2.0012} \text{ (dB/cm)} \tag{2}$$

$$c_s = \frac{c_w}{1 + \frac{\Delta t}{\Delta x} c_w} \tag{3}$$

$$c_w = 1402.9 + 4.835T - 0.047016T^2 + 0.00012725T^3 \tag{4}$$

where α_w and C_w are the acoustic attenuation coefficient and speed of sound of water [54,55], Δt is the difference in arrival time between the TMM and reference samples, Δx is the sample thickness (between the flask inner walls), and T denotes temperature in Kelvin. This substitution approach cancels out acoustic transfer characteristics of the flask walls, assuming that differences in acoustic impedances between the gel and water were small enough that differences in transmission coefficients could be neglected [32]. Power laws $\alpha(f) = af^n$ were fit to attenuation coefficient measurements over the usable band of frequencies for the transducers, typically 8–24 MHz. The power law fits were very close to the data in this frequency range (frequency-averaged root mean square difference = 0.05 ± 0.01 dB/cm for the measured samples) and could be extrapolated with high confidence throughout the usable band of the PAM system.

TMM optical properties were characterized using an integrating sphere spectrophotometer (Lambda1050, PerkinElmer, Waltham, MA). PAA was molded into disks with 40-mm diameter and nominal 1.7-mm thickness, which were placed between two 50 mm × 70 mm × 1 mm thick glass slides. Actual sample thickness was measured using digital calipers (IDC112TB, Mitutoyo, Kanagawa, Japan). Total transmittance and diffuse reflectance spectra were measured over

400–1100 nm, and measurements were calibrated using Spectralon 99% reflectance standards (Labsphere, Sutton, NH). μ_a and μ'_s spectra were computed from transmittance and reflectance using the well-established Inverse Adding-Doubling (IAD) algorithm [56]. IAD requires knowledge of the refractive index (n) and scattering anisotropy (g); the refractive index of clear PAA samples was measured as 1.39 at 589.3 nm using a digital refractometer (PA202, MISCO, Solon, OH) and g was estimated to be 0.65 based on Mie scattering calculations for 20–5000 nm diameter TiO$_2$ particles suspended in water ($n_{TiO_2} \sim 2.1$, $n_{H_2O} = 1.33$) [57]. It has been previously reported that IAD outputs are fairly insensitive to uncertainty in g [56], and varying g from 0.65 to 0.9 caused less than 3% change in μ_a and μ'_s in our study.

2.3. PAM image quality phantoms

We constructed two types of phantoms for PAM image quality testing – a "spatial resolution" phantom and a "penetration" phantom. Spatial resolution phantoms were prepared for each TMM recipe (Table 2) by molding a 40 mm diameter, 5 mm thick disk shape of PAA TMM that contained 0.15 µg/ml of 100 nm diameter gold nanospheres (AuNS) (A11-100, Nanopartz, Loveland, CO) (Fig. 2). This AuNS diameter was selected to achieve an absorption peak near the 570 nm operating wavelength of our PAM system and thus maximize photoacoustic signal generation efficiency. Resolution was evaluated by imaging a USAF 1951 target (#64–862, Edmund Optics, Barrington, NJ) placed at the system's optical focus using three different methods: 1) identification of the smallest discernible bar target by subjective inspection [21–23], 2) measuring the edge spread function (ESF) of a bright square target and computing the full-width half maximum (FWHM) of its derivative (the line spread function) [25,26,39], and 3) measuring contrast transfer function (CTF) across the bars [21,22]. Penetration phantoms were prepared by pouring PAA into a 20 mm × 20 mm × 20 mm acrylic mold containing two ~ 11°-slanted linear targets: a 25-µm diameter tungsten filament (10405, Alfa Aesar) and a 280/610-µm (ID/OD) polyethylene (PE) tube (PE10, Braintree Scientific, Inc., Braintree, MA). PE tubing was selected from among other tested tubes, including Tygon (TYG 030, Braintree Scientific, Braintree, MA), silicone rubber (SIL 025, Braintree Scientific), and PTFE (STT-30 Component Supply Company, Fort Meade, FL) as PE tubes produced greatest PA signal amplitudes when filled with blood (data not shown) (7230801, LAMPIRE Biological Laboratories, Pipersville, PA). Two metal bars were inserted into holes on the two sides to serve as stoppers of a plug lid (Fig. 2).

2.4. PAM image acquisition and analysis

The phantoms were used to characterize performance of a custom PAM imaging system shown in Fig. 3, which is based on a previously reported design [58]. The light source is a tunable dye laser (Credo-Dye-LG-24, Sirah Lasertechnik, Grevenbroich, Germany) that was operated at 570 nm, which is an isosbestic wavelength of hemoglobin and thus ensures PAM image contrast is independent of blood oxygenation. A single-mode fiber guides the beam into an imaging head comprised of a lens pair with a numerical aperture of 0.18 in air (#49–949, Edmund Optics), a custom acoustic-optical beam combiner made of two epoxy-glued right-angle prisms (#32–331, Edmund Optics) [58], an acoustic lens (#45–008, Edmund Optics), and a 50 MHz center frequency ultrasound transducer (V214-BB-RM, Olympus). Received photoacoustic signals were amplified using two low-noise amplifiers connected in series with a total gain of 56 dB (ZFL-500LN+, Mini-circuits, Inc., Brooklyn, NY), then digitized by an 8-bit DAQ device (PCI-5114, National Instruments, Inc.). Images were formed by raster scanning the imaging head using a fast-axis voice coil linear stage (VCS-10, Equipment Solutions, Inc., Forestville, CA) and a slow-axis stepper motor (X-LSM025A, Zaber Technologies, Inc., Vancouver, British Columbia, Canada). The voice coil motor was triggered by sinusoidal driving signals, and a built-in position sensor was used to calibrate image pixel intervals with a resolution of 0.15 µm. System operation
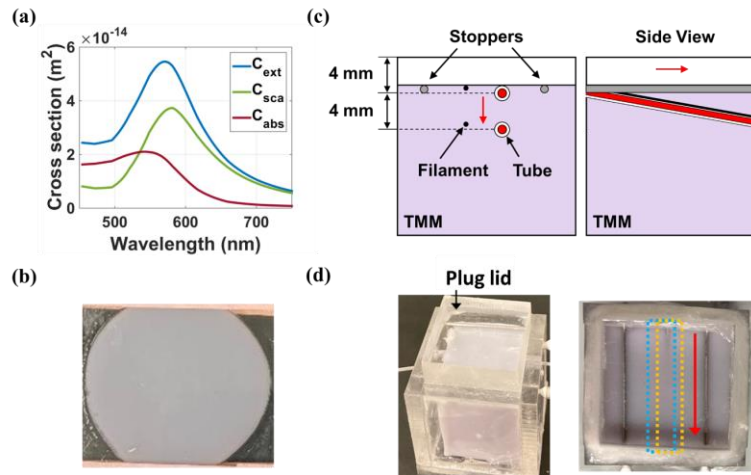
Fig. 2. (a) Optical extinction (C_{ext}), scattering (C_{sca}), and absorption (C_{abs}) cross-sections of gold nanospheres used in the spatial resolution phantom. (b) Photograph of a spatial resolution phantom composed of "high" TMM. (c) Diagram of penetration phantom design, showing position of slanted targets. (d) Photographs of the penetration phantom mold with and without the plug lid (with low TMM). Red arrows in (c) & (d) indicate PAM slow-axis scanning direction.

and synchronization were managed using a custom LabVIEW program (National Instruments) and a multifunctional I/O device (USB 6211, National Instruments).
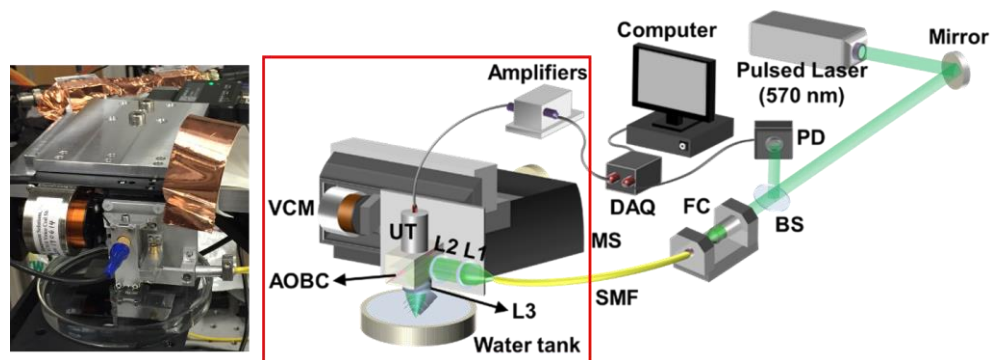
Fig. 3. Schematic of custom-built PAM system. L1, L2, L3, optical lenses; PD, photodiode; BS, beam sampler; FC, fiber coupler; SMF, single-mode fiber; DAQ, data acquisition unit; VCM, voice coil motor; MS, motorized stage; UT, ultrasonic transducer; AOBC, acoustic-optical beam combiner. Photo on the left shows the imaging probe (red square).

PAM volumetric images were acquired within a mean duration of 100 seconds at a 10 kHz laser pulse repetition rate. The per-pulse radiant exposure was 3.4 ± 0.15 µJ/cm^2 as measured over a beam diameter of 5.2 ± 0.16 mm. To compare exposure against standard safety limits specified by ANSI Z136.1:2014, radiant exposure was also computed over a 3.5 mm limiting aperture as 7.3 ± 0.32 µJ/cm^2, which is below the safety limit of 20 µJ/cm^2 (0.2 W/cm^2 / 10 kHz for repeated exposures) [59]. The voice coil motor was set to achieve a 10 Hz B-scan rate. Spatial
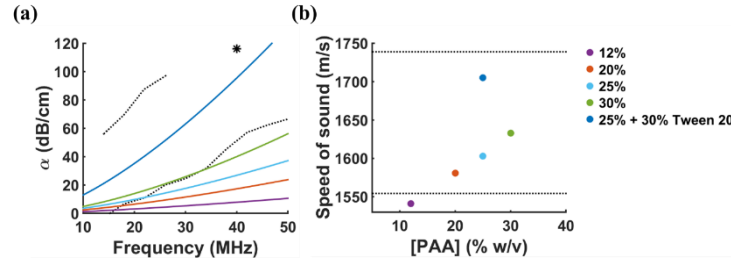
Fig. 4. Measured acoustic attenuation coefficient (a) and speed of sound (b) of PAA-based TMMs. Coefficient of variation < 5% for attenuation coefficient and < 0.2% for speed of sound. Black dashed lines and asterisk indicate the range reported in the literature (Fig. 1(c)) [46,47].

resolution phantoms were imaged with a 0.25 nm raster scanning step size over a 250 μm × 250 μm lateral field of view. The phantom was imaged in up to five distinct 150 μm × 150 μm regions, and two C-scans at each of six equally spaced depths down to 300 μm were acquired at each region with phantom vertical position adjusted via a translational stage. Penetration phantoms were imaged with a 1 μm fast-axis step size and 10 μm slow-axis step size to continuously record signal transition over depth. Filament and tube targets were aligned with the slow-axis scanning direction, automatically adjusting phantom vertical position with a translational stage during C-scan acquisition to maintain optical focus at the target as its depth increased.

Image processing was performed with uncompressed volumetric radiofrequency (RF) data. A-lines were converted to unipolar signal envelope through Hilbert transform, and maximum amplitude projection (MAP) was applied to C-scan data to produce top-view images. Image depth was calibrated using TMM speed of sound values. Spatial resolution was measured using FWHM of line profiles across a particle in top-view or unipolar B-scan images. To quantify maximum imaging depth, rectangular region of interests (ROIs) with dimensions 20 mm × 1.2 times the filament and tube width (30 μm and 340 μm, respectively) were drawn over the target object in MAP images and a background region of equal size located three target widths laterally from the target ROI, and the following parameters were measured. Target signal-to-noise (SNR), contrast-to-noise (CNR), and contrast ratio (CR) were computed using the following definitions:

$$SNR = \frac{S}{\sigma_B} \qquad\qquad CR = \frac{S}{B} \qquad\qquad CNR = \frac{S - B}{\sigma_B} \qquad\qquad (5)$$

where S is the mean pixel amplitude of the target ROI, B is the mean pixel amplitude of the background ROI, and is the standard deviation of the background ROI. Maximum imaging depth with respect to each metric was defined as the depth where the metric reached a threshold of 2 (6 dB).

3. Results

3.1. TMM acoustic and optical properties

As shown in Fig. 4, both α and c_s were positively correlated with PAA concentration. Acoustic attenuation increased nonlinearly with frequency for PAA concentration above 20%, and 30% PAA gels yielded attenuation similar to the lower range of reported values for human dermis [46,47]. It has been shown that adding viscous liquids such as corn syrup can increase both α and c_s in PAA hydrogels [60], and we observed a similar trend when adding viscous Tween 20. PAA gels containing 30% Tween 20 produced frequency-dependent acoustic attenuation of

$(0.27 \pm 0.07) f^{(1.5 \pm 0.03)}$, which was in the middle of the literature range, and speed of sound in the higher end of the literature range (1704 ± 2.72 m/s).

Figure 5(a, b) shows μ_a, μ'_s spectra and μ_a (570 nm), μ'_s (570 nm) values vs. nigrosin and TiO_2 nanopowder concentration from 400–1100 nm. Strong linearity at 570 nm vs. concentration was observed, with coefficient of determination (R^2) 0.99 for μ_a and $R^2 = 0.98$ for μ'_s, and the range of achieved values fully spanned our range of target TMM optical properties (Table 1). Adding Tween 20 to PAA resulted in significant increases in scattering even without TiO_2 (Fig. 5(c)). The dependence of optical properties at 570 nm on Tween 20 concentration also showed strong linearity, with $R^2 = 0.92$ for μ_a and $R^2 = 0.99$ for μ'_s. The addition of Tween 20 as well as bath sonication was effective in reducing TiO_2 aggregation, as determined by bright-field microscopy (Fig. 5(d)). PAA samples containing 30% v/v Tween 20 presented TiO_2 micro-aggregates with sizes smaller than 5 µm, in contrast to larger agglomerates in a sample containing 10% Tween 20. Similar turbidity has been reported in copolymerization of hydrogels and surfactants, which may result from high concentrations of formed micelles [61]. However, this level of scattering was still lower than target values, so TiO_2 could be added to achieve target properties.
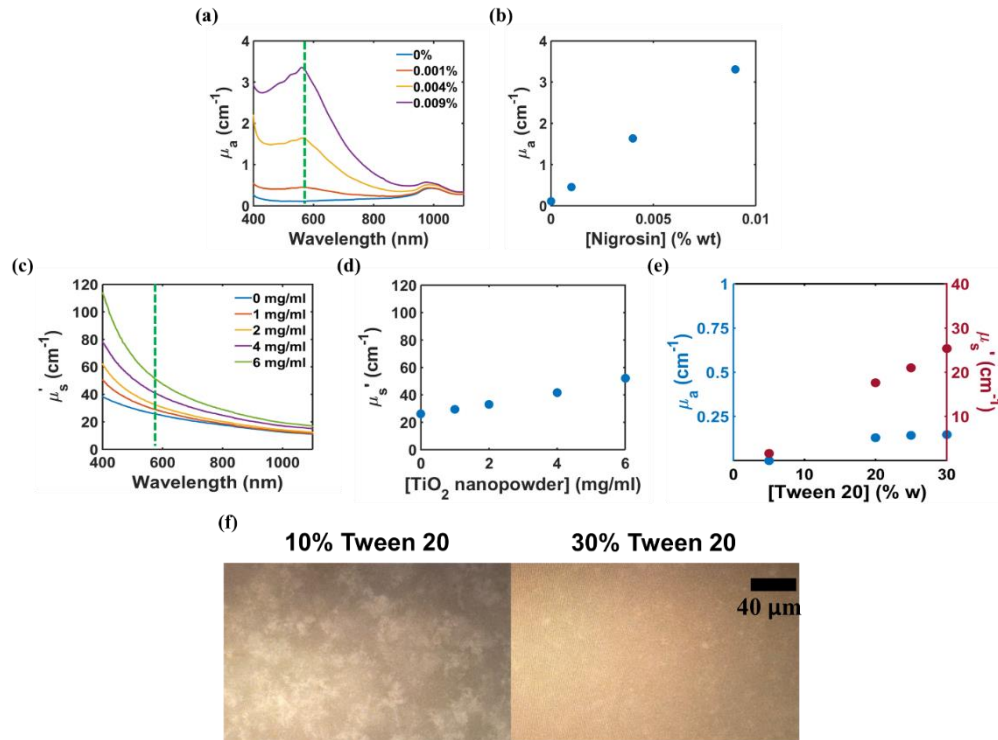

Fig. 5. Optical characterization of PAA TMMs. (a) μ_a spectra and (b) $\mu_a(570\ nm)$ vs. nigrosin concentration. (c) μ'_s spectra and (d) $\mu'_s(570\ nm)$ vs. TiO_2 concentration. Green dashed lines show PAM system wavelength of 570 nm. (e) $\mu_a(570\ nm)$ and $\mu'_s(570\ nm)$ v.s. Tween 20 concentration. (f) Bright-field microscopy images of PAA samples containing TiO_2 at different Tween 20 concentrations.

3.2. Resolution phantom testing

Figure 6 shows representative PAM images and resolution measurements using three USAF target-based methods and the PAA-based spatial resolution phantom. The wide-field image in

Fig. 6(d) shows that AuNSs were well dispersed in the phantom and a sufficient quantity of nanoparticles was available throughout the field of view for image quality analysis. Table 3 shows resolution measurement with USAF target and AuNS phantoms using the four methods (USAF inspection, USAF ESF, USAF CTF, and AuNS PSF). The measured lateral resolution was slightly higher than the system's optical diffraction limit of 1.62 μm [5]. The axial resolution measured with the AuNS PSF phantoms was also slightly higher than that obtained using the USAF target. AuNS PSF measurements showed higher uncertainty than USAF measurements, which may have been due to variations in fluence distribution (and thus SNR) within the field of view, nanoparticle polydispersity, or nanoparticle aggregation (see Fig. 6(c)). We noticed that resolution did not vary significantly with depth (data not shown), which was expected because optical scattering and acoustic attenuation are weak over the short pathlengths used in PAM within the quasi-ballistic regime ($1/\mu'_s \approx 450$ μm for the high TMM, for which $\alpha_{30\ MHz} \approx 2.7$ dB, Fig. 4). In addition, we did not observe lateral position-dependent variation in resolution (data not shown), which implies the PAM system's motor positioning precision exceeded the imaging resolution. AuNSs could only be detected at depths less than ~ 200 μm for all three TMMs, despite observing greater maximum imaging depth in phantoms containing blood-filled tubes. In addition to the well-known strong decrease in fluence with depth in turbid media, this observation might also be attributed to the relatively low absorption cross-section of a single nanoparticle versus the stronger absorption of highly concentrated hemoglobin molecules in red blood cells within the PAM optical focal region. Single nanoparticles may also be more sensitive to small changes in local fluence given their high surface area and lack of adjacent competing absorbers (as is the case in blood).

Table 3. Resolution Measurements with USAF Target and AuNS Phantoms.

Resolution (μm)	USAF Inspection	USAF ESF/LSF	USAF CTF	AuNS (Low TMM)	AuNS (Medium TMM)	AuNS (High TMM)
Lateral	1.95	2.2 ± 0.2	3.1	2.5 ± 0.4	2.4 ± 0.5	2.8 ± 0.5
Axial	—	33.5 ± 2.7	—	42.5 ± 3.3	45.7 ± 6.0	43.3 ± 6.9

3.3.   Penetration phantom testing

Top-view maximum amplitude projection (MAP) images of the medium TMM phantom (Fig. 7(a)) show that the tungsten filament appeared brighter and longer (and thus was detected at greater depths) than the blood-filled tube. This difference in detectability may be attributed to the higher absorption coefficient ($\sim 5000\times$) and Gruneisen parameter ($\sim 10\times$) of tungsten vs. blood [62–65]. In cross-sectional B-scan images, the tungsten filament appeared as a bright vertical ellipsoid as its diameter is smaller than the system's axial resolution but larger than the lateral resolution (Fig. 7(b)). In contrast, the tube appeared as a large, crescent-shaped feature that corresponded to its top wall, which is likely due to a combination of boundary buildup effect caused by finite transducer bandwidth, limited view artifacts caused by the scanning geometry, and fluence decreases with depth caused by intra-target attenuation within the tube lumen.

As shown in Fig. 8, SNR, CR, and CNR all decreased with increasing target depth as well as with increasing TMM optical attenuation. For depths less than 300 μm, the tungsten filament was more detectable than the tube, with approximately 2.5–3 times higher SNR, CR, and CNR. Additionally, metrics for the tube target presented twice the standard deviation vs. filament metrics. This may have been due to nonuniform amplitude of tube target features caused by limited view effects, as pixels near the sides of the tube (and included in ROIs) had significantly lower amplitudes. Tungsten filaments were detected at greater depths than blood-filled tubes (Fig. 9), primarily due to higher target image amplitude rather than differences
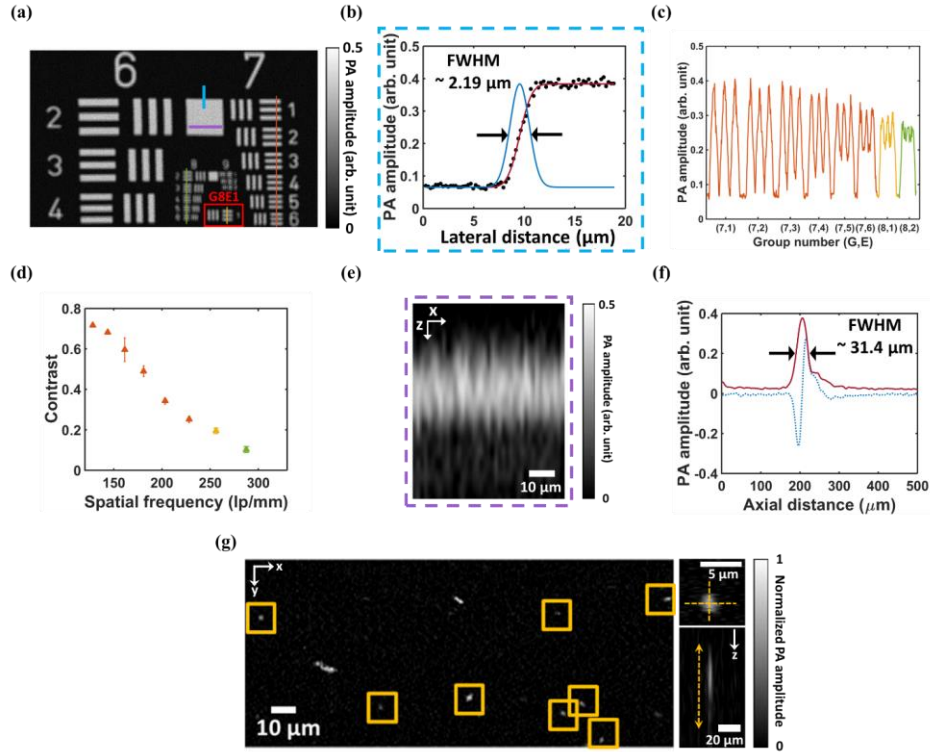
Fig. 6. (a) Top-view PAM image of an USAF target in water. (b) Lateral resolution measurement using edge spread function fitting in lateral direction. The smallest resolvable line pair based on inspection was Group 8, Element 1 (red box). (c) PA intensity profiles across lines in the top-view image. (d) CTF reveals a cutoff spatial frequency of 320 lp/mm, which corresponds to a resolution of 3.1 μm. (e) Hilbert transformed B-scan image of the selected (purple) region. (f) Axial resolution measurement using the averaged A-line profile from the B-scan image. (g) PAM image of the spatial resolution phantom with the high TMM formulation and selected regions for quantitative measurements of lateral (upper right) and axial (lower right) resolution.
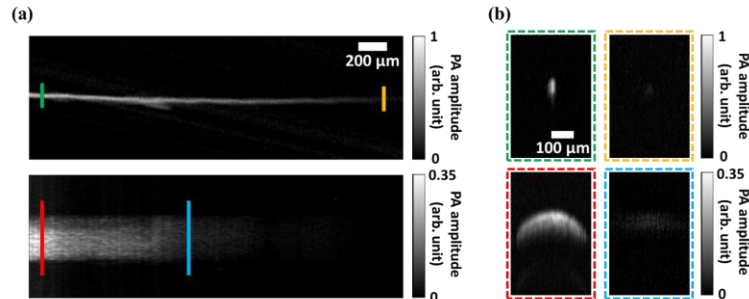

Fig. 7. (a) Representative top-view MAP images of a tungsten filament (top) and blood-filled tube (bottom) in the medium TMM penetration phantom. (b) Cross-sectional images of the two targets at 100 μm depth and depths where CNR ≈ 2 (6 dB). Image outline colors in (b) correspond to colored lines in (a).
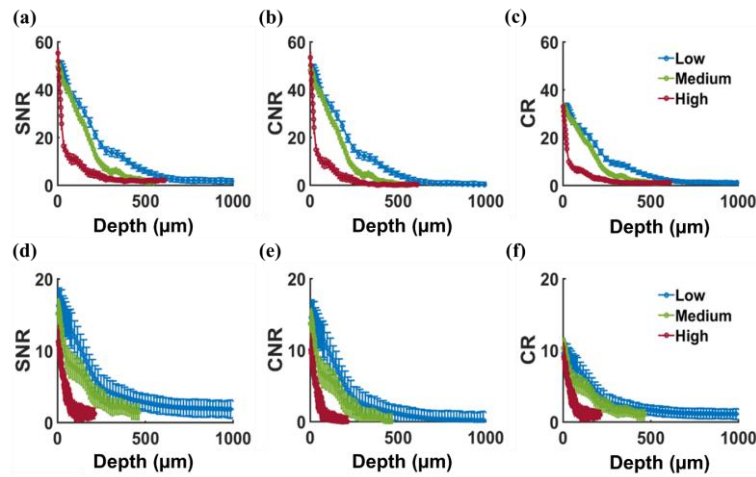
Fig. 8. SNR, CNR, and CR of tungsten filament (a – c) and blood-filled tube (d – f) in low, medium, and high optical attenuation TMMs.
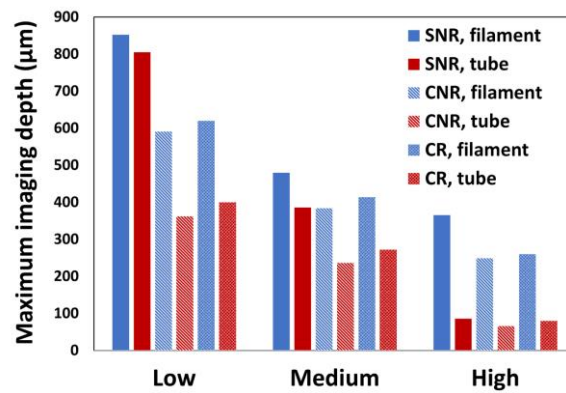

Fig. 9. Maximum imaging depth as determined using SNR, CNR, and CR (6 dB threshold) for the tungsten filament and blood-filled tube in low, medium, and high optical attenuation TMMs.

in image background amplitude or variation. Of the three image quality metrics evaluated, SNR yielded the largest maximum imaging depth based on a threshold of 6 dB, followed by CR and then CNR. This may have resulted from the use of a constant detection threshold (6 dB) for each metric. These metrics are clearly correlated based on their definitions, as evidenced by the relationship CNR = SNR(1-1/CR) [32], but a value of 6 dB has different meaning for each metric. For example, under the condition CR = 2 (6 dB) and SNR = 2 (6 dB), CNR = 1 (0 dB). CNR represents a more comprehensive metric, while CR is a simpler but acceptable metric when the image background is dark and has low noise. Interestingly, the filament and tube were both detectable to greater depths than the single gold nanoparticles used in the spatial resolution phantom. This difference may be attributed to relatively weaker photoacoustic signals detected from a single nanoparticle, as opposed to cylindrical targets with larger dimensions and/or higher absorption coefficient.

4.   Discussion and conclusions

Our results demonstrate that our developed TMM is tunable, biologically relevant, and suitable for constructing phantoms that enable quantitative performance assessment of PAM image quality. TMM optical and acoustic properties overlapped with reported values from the literature. Our TMM and phantoms developed specifically for PAM applications differ significantly from common phantom designs used to evaluate macroscopic PAI systems [32,34,35,39,66]. First, this novel TMM was formulated to achieve bio-relevant acoustic attenuation at high frequencies relevant to PAM but typically not characterized in TMMs used for macro-PAI. Second, the TMM was formulated with a surfactant and characterized by bright-field microscopy to improve microscopic homogeneity necessary for consistent evaluation of PAM systems (especially regarding reproducible dispersion of suspended particles such as TiO_2). Finally, while many macro-PAI phantoms use arrays of several horizontal tubes located at different depths, our PAM phantom used a single vertically slanted tube. This design allows finer and simpler characterization of depth-dependent performance over the much shallower imaging depths (~ 1 mm) compared to macro-PAI (~ 3–4 cm). The traditional tube array design used in macro-PAI phantoms would be difficult to implement within the shallow imaging depth of PAM due to challenges in positioning several tubes with sub-millimeter accuracy and in close proximity (which would likely be needed to maximize number of targets in the field of view and minimize scan time).

Spatial resolution phantoms containing dispersed nanoparticles as point targets allowed characterization of resolution in three dimensions. Unlike tests using a USAF 1951 target, this PSF-based phantom design enables 3D resolution measurements at multiple depths and lateral positions in a single scan. Nanoparticles were detected to depths of 200 µm, but phantom utility may be optimized by embedding nanoparticles with higher absorption cross-section at system-relevant wavelengths. These phantoms may also be useful for assessing depth-dependent detectability of specific nanoparticles relevant to a given application. While many literature studies reported PAM resolution testing in minimally attenuating media such as water baths (Section 1), we applied a test paradigm focused on estimating real-world performance, rather than evaluating best-case performance. Notably, nanoparticle-based phantoms have been used to evaluate resolution of optical coherence tomography systems, although these approaches used a transparent phantom to evaluate ideal resolution [67]. Both idealized and biologically relevant phantom approaches can be useful for device development and performance evaluation, although the differences in intended purpose and limitations of these approaches should be carefully considered.

Test results from nanoparticle, filament, and tube measurements illustrated that the maximum imaging depth of a PAM system is highly dependent on the imaging target. Tungsten filaments were detected at greatest depths, followed by blood-filled tubes and then nanoparticles. This result was expected as 1) metal filaments typically have higher absorption coefficient and Gruneisen parameter than blood, and 2) individual nanoparticles possess fairly low absorption cross-section [62,63]. Other studies have reported maximum imaging depth of PAM systems using many different approaches (see Section 1), but our results suggest that values measured using metal filaments or carbon fibers may overestimate useful imaging depth when the device's primary application is to detect lower contrast targets such as blood vessels or nanoparticles. Filaments may be suitable for estimating resolution but may not be suitable for imaging depth or detectability testing unless the specific imaging application involves detection of embedded metal objects. While tubes may present a thicker wall and different acoustic properties compared to blood vessel, they offer an economic and convenient approach for placing contrast media such as blood within a phantom. In addition to choice of imaging target, measured imaging depth also depended on the optical and acoustic properties of the phantom background material. Because the properties of

ex vivo tissue and phantoms are often not reported, this may introduce considerable uncertainty into reported imaging depth results.

Finally, imaging depth test results depended on data analysis methods and choice of image quality metrics. Selection of image quality metrics (SNR, CR, or CNR), pre-defined detection threshold (e.g., 6 dB), or ROI dimensions may significantly affect quantitative test results. Our results showed that analysis based on SNR produced greater values of maximum imaging depth, while CR and CNR produced lower and more similar values. This was perhaps because each analysis used a cutoff detection threshold of 2, which has slightly different meaning for each metric, or because CR and CNR consider the difference in target and background amplitudes, while SNR does not (instead comparing signal amplitude against background standard deviation). The observed variations in image quality test results highlights the context-sensitive nature of maximum imaging depth, which depends on imaging target geometry and material properties as well as image analysis methodology. This observation may also apply to other image quality characteristics of PAM systems.

In conclusion, we developed a polyacrylamide-based, dermis-mimicking TMM specifically optimized for PAM applications and demonstrated tunability of its optical and acoustic properties. We constructed phantoms from these TMMs to assess image quality of a custom-built OR-PAM system. To ensure consistent and reproducible PAM image quality test results, we recommend that reported image quality specifications for PAM systems, such as resolution and maximum imaging depth, be accompanied by a description of 1) the test phantom optical and acoustic properties, 2) the properties and geometry of embedded imaging targets, and 3) the specific metrics and analysis methods used to quantify the results. Development of standardized consensus test methods would improve comparability of reported results and reduce burden on developers to design their own test methods. These phantom test methods may be useful tools that can facilitate PAM device characterization and optimization, accelerate clinical translation, support regulatory evaluation, and lay foundations for future development of standardized performance test methods.

References

1. A. B. E. Attia, G. Balasundaram, M. Moothanchery, U. S. Dinish, R. Bi, V. Ntziachristos, and M. Olivo, "A review of clinical photoacoustic imaging: Current and future trends," Photoacoustics **16**, 100144 (2019).
2. J. Yao and L. V. Wang, "Recent progress in photoacoustic molecular imaging," Curr. Opin. Chem. Biol. **45**, 104–112 (2018).
3. J. Zhang, F. Duan, Y. Liu, and L. Nie, "High-resolution photoacoustic tomography for early-stage cancer detection and its clinical translation," Radiol. Imaging Cancer **2**(3), e190030 (2020).
4. D. Das, A. Sharma, P. Rajendran, and M. Pramanik, "Another decade of photoacoustic imaging," Phys. Med. Biol. **66**(5), 05TR01 (2021).
5. L. V. Wang and S. Hu, "Photoacoustic Tomography: In vivo imaging from organelles to organs," Science **335**(6075), 1458–1462 (2012).
6. W. Choi, E. Y. Park, S. Jeon, and C. Kim, "Clinical photoacoustic imaging platforms," Biomed. Eng. Lett. **8**(2), 139–155 (2018).
7. FDA Databases, https://www.accessdata.fda.gov/scripts/cdrh/cfdocs/cfpma/pma.cfm?id=P200003. (Accessed 14 Jan. 2022).

8. Z. Cheng, H. Ma, Z. Wang, and S. Yang, "In vivo volumetric monitoring of revascularization of traumatized skin using extended depth-of-field photoacoustic microscopy," Front. Optoelectron. **13**(4), 307–317 (2020).

9. M. Seong and S. L. Chen, "Recent advances toward clinical applications of photoacoustic microscopy: a review," Sci. China Life Sci. **63**(12), 1798–1812 (2020).

10. S. Jeon, J. Kim, D. Lee, J. W. Baik, and C. Kim, "Review on practical photoacoustic microscopy," Photoacoustics **15**, 100141 (2019).

11. T. T. W. Wong, R. Zhang, P. Hai, C. Zhang, M. A. Pleitez, R. L. Aft, D. V. Novack, and L. V. Wang, "Fast label-free multilayered histology-like imaging of human breast cancer by photoacoustic microscopy," Sci. Adv. **3**(5), e1602168 (2017).

12. B. Park, C. H. Bang, C. Lee, J. H. Han, W. Choi, J. Kim, G. S. Park, J. W. Rhie, J. H. Lee, and C. Kim, "3D wide-field multispectral photoacoustic imaging of human melanomas in vivo: a pilot study," J. Eur. Acad. Dermatol. Venereol. **35**(3), 669–676 (2021).

13. A. Cebrecos, J. J. Garcia-Garrigos, A. Descals, N. Jimenez, J. M. Benlloch, and F. Camarena, "Beamforming for large-area scan and improved SNR in array-based photoacoustic microscopy," Ultrasonics **111**, 106317 (2021).

14. T. Jin, H. Guo, H. Jiang, B. Ke, and L. Xi, "Portable optical resolution photoacoustic microscopy (pORPAM) for human oral imaging," Opt. Lett. **42**(21), 4434–4437 (2017).

15. J. Yao, C.-H. Huang, L. Wang, J.-M. Yang, L. Gao, K. I. Maslov, J. Zou, and L. V. Wang, "Wide-field fast-scanning photoacoustic microscopy based on a water-immersible MEMS scanning mirror," J. Biomed. Opt. **17**(8), 080505 (2012).

16. American College of Radiology, "Computed tomography: quality control manual," https://www.acr.org/-/media/ACR/Files/Clinical-Resources/QC-Manuals/CT_QCManual.pdf (2017).

17. American College of Radiology, Computed Tomography Accreditation Program, "Phantom testing: CT," https://accreditationsupport.acr.org/support/solutions/articles/11000056197-acr-ct-phantom-scanning-instructions (2019).

18. C. H. McCollough, M. R. Bruesewitz, M. F. McNitt-Gray, K. Bush, T. Ruckdeschel, J. T. Payne, J. A. Brink, and R. K. Zeman, "The phantom portion of the American College of Radiology (ACR) Computed Tomography (CT) accreditation program: Practical tips, artifact examples, and pitfalls to avoid," Med. Phys. **31**(9), 2423–2442 (2004).

19. P. Hai, J. Yao, K. I. Maslov, Y. Zhou, and L. V. Wang, "Near-infrared optical-resolution photoacoustic microscopy," Opt. Lett. **39**(17), 5192–5195 (2014).

20. H. M. Heres, M. U. Arabul, M. C. M. Rutten, F. N. Van de Vosse, and R. G. P. Lopata, "Visualization of vasculature using a hand-held photoacoustic probe: phantom and in vivo validation," J. Biomed. Opt. **22**(4), 041013 (2017).

21. S. Hu, K. I. Maslov, and L. V. Wang, "Second-generation optical-resolution photoacoustic microscopy with improved sensitivity and speed," Opt. Lett. **36**(7), 1134–1136 (2011).

22. M. Moothanchery and M. Pramanik, "Performance characterization of a switchable acoustic resolution and optical resolution photoacoustic microscopy system," Sensors **17**(2), 357 (2017).

23. G. Ku, K. I. Maslov, L. Li, and L. V. Wang, "Photoacoustic microscopy with 2-μm transverse resolution," J. Biomed. Opt. **15**(2), 021302 (2010).

24. L. Wang, K. I. Maslov, J. Yao, B. Rao, and L. V. Wang, "Fast voice-coil scanning optical-resolution photoacoustic microscopy," Opt. Lett. **36**(2), 139–141 (2011).

25. J. Y. Kim, C. Lee, K. Park, G. Lim, and C. Kim, "Fast optical-resolution photoacoustic microscopy using a 2-axis water-proofing MEMS scanner," Sci. Rep. **5**(1), 7932 (2015).

26. W. Qi, Q. Chen, H. Guo, H. Xie, and L. Xi, "Miniaturized optical resolution photoacoustic microscope based on a microelectromechanical systems scanning mirror," Micromachines **9**(6), 288 (2018).

27. L. Wang, K. I. Maslov, W. Xing, A. Garcia-Uribe, and L. V. Wang, "Video-rate functional photoacoustic microscopy at depths," J. Biomed. Opt. **17**(10), 1 (2012).

28. C. Lee, D. Lee, Q. Zhou, J. Kim, and C. Kim, "Real-time near-infrared virtual intraoperative surgical photoacoustic microscopy," Photoacoustics **3**(3), 100–106 (2015).

29. J. Chen, Y. Zhang, S. Bai, J. Zhu, P. Chirarattananon, K. Ni, Q. Zhou, and L. Wang, "Dual-foci fast-scanning photoacoustic microscopy with 3.2-MHz A-line rate," Photoacoustics **23**, 100292 (2021).

30. J. Laufer, E. Zhang, and P. Beard, "Evaluation of absorbing chromophores used in tissue phantoms for quantitative photoacoustic spectroscopy and imaging," IEEE J. Sel. Top. Quantum Electron. **16**(3), 600–607 (2010).

31. A. I. Chen, M. L. Balter, M. I. Chen, D. Gross, S. K. Alam, T. J. Maguire, and M. L. Yarmush, "Multilayered tissue mimicking skin and vessel phantoms with tunable mechanical, optical, and acoustic properties," Med. Phys. **43**(6Part1), 3117–3131 (2016).

32. A. Hariri, J. Palma-Chavez, K. A. Wear, T. J. Pfefer, J. V. Jokerst, and W. C. Vogt, "Polyacrylamide hydrogel phantoms for performance evaluation of multispectral photoacoustic imaging systems," Photoacoustics **22**, 100245 (2021).

33. J. Joseph, M. R. Tomaszewski, I. Quiros-Gonzalez, J. Weber, J. Brunker, and S. E. Bohndiek, "Evaluation of precision in optoacoustic tomography for preclinical imaging in living subjects," J. Nucl. Med. **58**(5), 807–814 (2017).

34. C. Avigo, N. Di Lascio, P. Armanetti, C. Kusmic, L. Cavigli, F. Ratto, S. Meucci, C. Masciullo, M. Cecchini, R. Pini, F. Faita, and L. Menichetti, "Organosilicon phantom for photoacoustic imaging," J. Biomed. Opt. **20**(4), 046008 (2015).

35. E. Maneas, W. Xia, O. Ogunlade, M. Fonseca, D. I. Nikitichev, A. L. David, S. J. West, S. Ourselin, J. C. Hebden, T. Vercauteren, and A. E. Desjardins, "Gel wax-based tissue-mimicking phantoms for multispectral photoacoustic imaging," Biomed. Opt. Express **9**(3), 1151–1163 (2018).

36. W. C. Vogt, C. Jia, K. A. Wear, B. S. Garra, and T. J. Pfefer, "Biologically relevant photoacoustic imaging phantoms with tunable optical and acoustic properties," J. Biomed. Opt. **21**(10), 101405 (2016).

37. E.-J. Jeong, H.-W. Song, Y.-J. Lee, S. J. Park, M. J. Yim, S. S. Lee, and B. K. Kim, "Fabrication and characterization of PVCP human breast tissue-mimicking phantom for photoacoustic imaging," BioChip J. **11**(1), 67–75 (2017).

38. J. R. Cook, R. R. Bouchard, and S. Y. Emelianov, "Tissue-mimicking phantoms for photoacoustic and ultrasonic imaging," Biomed. Opt. Express **2**(11), 3193–3206 (2011).

39. J. Palma-Chavez, T. J. Pfefer, A. Agrawal, J. V. Jokerst, and W. C. Vogt, "Review of consensus test methods in medical imaging and current practices in photoacoustic image quality assessment," J. Biomed. Opt. **26**(09), 1–27 (2021).

40. Y. Shimojo, T. Nishimura, H. Hazama, T. Ozawa, and K. Awazu, "Measurement of absorption and reduced scattering coefficients in Asian human epidermis, dermis, and subcutaneous fat tissues in the 400- to 1100-nm wavelength range for optical penetration depth and energy deposition analysis," J. Biomed. Opt. **25**(04), 1 (2020).

41. C. R. Simpson, M. Kohl, M. Essenpreis, and M. Cope, "Near-infrared optical properties of ex vivo human skin and subcutaneous tissues measured using the Monte Carlo inversion technique," Phys. Med. Biol. **43**(9), 2465–2478 (1998).

42. E. Salomatina, B. Jiang, J. Novak, and A. N. Yaroslavsky, "Optical properties of normal and cancerous human skin in the visible and near-infrared spectral range," J. Biomed. Opt. **11**(6), 064026 (2006).

43. N. Bosschaart, R. Mentink, Joke H Kok, Ton G van Leeuwen, and M. C. G. Aalders, "Optical properties of neonatal skin measured in vivo as a function of age and skin pigmentation," J. Biomed. Opt. **16**(9), 097003 (2011).

44. A. N. Bashkatov, E. A. Genina, V. I. Kochubey, and V. V. Tuchin, "Optical properties of human skin, subcutaneous and mucous tissues in the wavelength range from 400 to 2000 nm," J. Phys. D Appl. Phys. **38**(15), 2543–2555 (2005).

45. L. Pan, L. Zan, and F. S. Foster, "Ultrasonic and viscoelastic properties of skin under transverse mechanical stress in vitro," Ultrasound Med. Biol. **24**(7), 995–1007 (1998).

46. B. I. Raju and M. A. Srinivasan, "High-frequency ultrasonic attenuation and backscatter coefficients of in vivo normal human dermis and subcutaneous fat," Ultrasound Med. Biol. **27**(11), 1543–1556 (2001).

47. C. Guittet, F. Ossant, L. Vaillant, and M. Berson, "In vivo high-frequency ultrasonic characterization of human dermis," IEEE Trans. Biomed. Eng. **46**(6), 740–746 (1999).

48. C. M. Moran, N. L. Bush, and J. C. Bamber, "Ultrasonic propagation properties of excised human skin," Ultrasound Med. Biol. **21**(9), 1177–1190 (1995).

49. N. Y. Abu-Thabit, "Thermochemistry of acrylamide polymerization: an illustration of auto-acceleration and gel effect," World J Chem. Educ. **5**(3), 94–101 (2017).

50. M. Radecki, J. Spěváček, A. Zhigunov, Z. Sedláková, and L. Hanyková, "Temperature-induced phase transition in hydrogels of interpenetrating networks of poly(N-isopropylacrylamide) and polyacrylamide," Eur. Polym. J. **68**, 68–79 (2015).

51. M. F. Cunningham, "Controlled/living radical polymerization in aqueous dispersed systems," Prog. Polym. Sci. **33**(4), 365–398 (2008).

52. K. A. Wear, "Mechanisms of interaction of ultrasound with cancellous bone: a review," IEEE Trans. Ultrason. Ferroelectr Freq. Control **67**(3), 454–482 (2020).

53. K. A. Wear, "Measurements of phase velocity and group velocity in human calcaneus," Ultrasound Med. Biol. **26**(4), 641–646 (2000).

54. M. J. Holmes, N. G. Parker, and M. J. W. Povey, "Temperature dependence of bulk viscosity in water using acoustic spectroscopy," J. Phys.: Conf. Ser. **269**, 012011 (2011).

55. G. W. C. Kaye and T. H. Laby, *Tables of physical and chemical constants* (Longman, 1995).

56. S. A. Prahl, M. J. C. van Gemert, and A. J. Welch, "Determining the optical properties of turbid media by using the adding–doubling method," Appl. Opt. **32**(4), 559–568 (1993).

57. J.-P. Jalava, V.-M. Taavitsainen, R.-J. Lamminmäki, M. Lindholm, S. Auvinen, M. Alatalo, E. Vartiainen, and H. Haario, "Modeling TiO2's refractive index function from bulk to nanoparticles," J. Quant. Spectrosc. Radiat. Transf. **167**, 105–118 (2015).

58. H. C. Hsu, L. Wang, and L. V. Wang, "In vivo photoacoustic microscopy of human cuticle microvasculature with single-cell resolution," J. Biomed. Opt. **21**(5), 056004 (2016).

59. "*American National Standard for safe use of lasers*," (Laser Institute of America, 2021).

60. S. R. Guntur and M. J. Choi, "An improved tissue-mimicking polyacrylamide hydrogel phantom for visualizing thermal lesions with high-intensity focused ultrasound," Ultrasound Med. Biol. **40**(11), 2680–2691 (2014).

61. T. Friedrich, B. Tieke, F. J. Stadler, and C. Bailly, "Copolymer hydrogels of acrylic acid and a nonionic surfmer: pH-induced switching of transparency and volume and improved mechanical stability," Langmuir **27**(6), 2997–3005 (2011).

62. W. S. M. Werner, K. Glantschnig, and C. Ambrosch-Draxl, "Optical constants and inelastic electron-scattering data for 17 elemental metals," J. Phys. Chem. Ref. Data **38**(4), 1013–1092 (2009).

63. M. Li, Y. Tang, and J. Yao, "Photoacoustic tomography of blood oxygenation: A mini review," Photoacoustics **10**, 65–73 (2018).

64. P. G. Grodzka, Gruneisen parameter study (Lockheed Missiles and Space Co. Inc. Huntsville Al. Huntsville Engineering Center, https://apps.dtic.mil/sti/citations/AD0786937, 1967).

65. E. Petrova, S. Ermilov, R. Su, V. Nadvoretskiy, A. Conjusteau, and A. Oraevsky, "Using optoacoustic imaging for measuring the temperature dependence of Grüneisen parameter in optically absorbing solutions," Opt. Express **21**(21), 25077–25090 (2013).

66. W. C. Vogt, C. Jia, K. A. Wear, B. S. Garra, and T. J. Pfefer, "Phantom-based image quality test methods for photoacoustic imaging systems," J. Biomed. Opt. **22**(9), 095002 (2017).

67. A. Fouad, T. J. Pfefer, C.-W. Chen, W. Gong, A. Agrawal, P. H. Tomlins, P. D. Woolliams, R. A. Drezek, and Y. Chen, "Variations in optical coherence tomography resolution and uniformity: a multi-system performance comparison," Biomed. Opt. Express **5**(7), 2066–2081 (2014).